3rd INTERNATIONAL SYMPOSIUM ON TWO-PHASE FLOW MODELLING AND EXPERIMENTATION

Pisa, Italy - September 22-25, 2004

Organized by

THE ASSEMBLY OF WORLD CONFERENCES ON EXPERIMENTAL HEAT TRANSFER, FLUID MECHANICS AND THERMODYNAMICS

the

ENEA INSTITUTE OF THERMAL-FLUID DYNAMICS

and the

DEPARTMENT OF ENERGETICS, UNIVERSITY OF PISA

with participation of the

JAPAN SOCIETY OF MULTIPHASE FLOW

Gas-Liquid phase distribution and void fraction measurements using the MRI

Daidžić N.E.[†], Schmidt E.[†], Montague I.[¶], Hasan M.M.[§], Altobelli S.[‡]

[†]National Center for Microgravity Research (NCMR), NASA John H. Glenn Research Center, 21000 Brookpark Rd., MS 110-3, Cleveland, OH 44135, U.S.A., Tel: 216-433-3270, Fax: 216-433-3793, Email: Nihad.Daidzic@grc.nasa.gov

[¶]Shaw University, 118 East South Street, Raleigh, NC 27601, U.S.A.

[§]NASA John H. Glenn Research Center, 21000 Brookpark Rd., MS 110-3, Cleveland, OH 44135, U.S.A.

[‡]New Mexico Resonance, 2301 Yale Blvd., SE; Suite C-1, Albuquerque, NM 87106-4237, U.S.A.

Keywords: Two-Phase, Gas-Liquid, Void fraction, MRI, Spin-Echo Imaging

Abstract

We are using a permanent-magnet MRI (Magnetic Resonance Imaging) with MRT spectrometer/imager to estimate the phase and void fraction distributions and flow patterns in gas-liquid two-phase flows. Air is being introduced at the bottom of the stagnant liquid column using accurate *Harvard Apparatus* programmable syringe pump PHD2000. Air flow rates were varied between 1 and 200 ml/min. The cylindrical non-conducting test tube of 2.5 cm diameter in which two-phase flow was measured was placed in a 10 cm diameter by 30 cm long solenoidal *radio-frequency (rf)* coil.

The MRI is based on a 1900 lbs (865 kg) NdFeB low-field (0.267T or 2670 Gauss) permanent magnet protected by the *Faraday* cage. Very low fringe (stray) magnetic field exists which minimizes the *rf* disturbances and relaxes the safety considerations. The static magnetic field is very homogeneous due to the large (110 cm) return pole pieces that also minimize stray field. The operating proton frequency is about 11.3 MHz, which is outside the public FM *rf* range (it is in the HF range). Homogeneous region of 8 cm DSV exists with the homogeneity of 25 ppm p-p. Clear access of 13.6 cm exists in which the measuring sample, gradient coils and the *rf* probe-transmitter is placed. The resistivity of the pole pieces is larger than 1.2 μOhm meter. The large magnet mass has a long temperature stabilization time and requires conditioned air with temperature control within 2-3 degrees Celsius for the stability of the static field. Intel Pentium PC computer with the I/O Texas Instrument TMS 320 C044 60 MHz DSP is used. Full functioning and flow imaging optimized Image-processing and spectroscopic analysis software is installed. Image processing software is based on IDL 5.6.

The air is transparent to NMR *rf* signal and only precessing ^{1}H protons induce *emf* in the receiving coil. Accordingly, we measure gas phase distribution indirectly. The spatial signal is compared to a test tube filled with water to extract the gas-phase distribution. Fast temporal measurements of phase distribution in tube cross-section(s) and time-averaged void fraction for the 2D and 3D domains in case of a steady flow have been achieved. For void fraction imaging and data acquisition we used *Hahn* spin-echo technique with spin echo times varying between 6-10 ms. Due to the relatively fast echo sequencing and low bubble velocities good spatial and temporal resolution was achieved. The characteristic voxel size was less than 500 μm (0.5 mm). The spatial resolution can be improved down to 100 μm, in which case the temporal resolution would suffer somewhat. In Figure below, the measured vertically-integrated cross-section void fraction distribution in a vertical test tube with stagnant liquid at 30 ml/min air flow rate is shown (void fraction is on the vertical axis).

MRI is a very promising technique for estimation of gas-liquid phase distributions, void fraction distributions, and flow patterns visualization in 2D or 3D domains for not too large flow velocities. A compromise has to be reached between the spatial and temporal resolution. MRI is especially well suited for 3D time-averaged volume-void-fraction measurements in case of steady two-phase flows. The beautiful thing with the MRI is that we can now add phase-contrast 3D velocity measurements by which independent closure of the mass and momentum balances can be obtained from the MRI measurements alone.

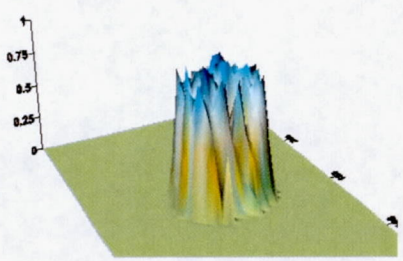

Gas-Liquid phase distribution and void fraction measurements using the MRI

Daidžić N.E.[†], **Schmidt E.**[†], **Hasan M.M.**[§], **Altobelli S.**[‡]

[†]National Center for Microgravity Research (NCMR), NASA John H. Glenn Research Center, 21000 Brookpark Rd., MS 110-3, Cleveland, OH 44135, U.S.A., Tel: 216-433-3270, Fax: 216-433-3793, Email: Nihad.Daidzic@grc.nasa.gov
[§]NASA John H. Glenn Research Center, 21000 Brookpark Rd., MS 110-3, Cleveland, OH 44135, U.S.A.
[‡]New Mexico Resonance, 2301 Yale Blvd., SE; Suite C-1, Albuquerque, NM 87106-4237, U.S.A.

ABSTRACT

We used a permanent-magnet MRI system to estimate the integral and spatially- and/or temporally-resolved void-fraction distributions and flow patterns in gas-liquid two-phase flows. Air was introduced at the bottom of the stagnant liquid column using an accurate and programmable syringe pump. Air flow rates were varied between 1 and 200 ml/min. The cylindrical non-conducting test tube in which two-phase flow was measured was placed in a 2.67 kGauss MRI with MRT spectrometer/imager. Roughly linear relationship has been obtained for the integral void-fraction, obtained by volume-averaging of the spatially-resolved signals, and the air flow rate in upward direction. The time-averaged spatially-resolved void fraction has also been obtained for the quasi-steady flow of air in a stagnant liquid column. No great accuracy is claimed as this was an exploratory proof-of-concept type of experiment. Preliminary results show that MRI a non-invasive and non-intrusive experimental technique can indeed provide a wealth of different qualitative and quantitative data and is especially well suited for averaged transport processes in adiabatic and diabatic multi-phase and/or multi-component flows.

INTRODUCTION

The knowledge of the instantaneous spatially-resolved or time-averaged, with or without spatial information, phase and void fraction distributions is a crucial information in characterization of the multi-phase and/or multi-component systems. The flow patterns can be evaluated by the knowledge of the phase distributions and much about the flow dynamics in adiabatic or diabatic conditions could be learned. The degree of complexity in understanding mass, momentum, and energy transfer processes in multi-phase and/or multi-component flows in various geometries is enormous. Therefore, it is essential to provide as much accurate experimental insight and relevant data to better understand the complex multi-phase flow phenomena and phase interactions.

Predictive CFD models rely on accurate and physically sound phenomenological relations, kinematic, and conservation principles for mass, momentum, and energy for each phase. CFD in gas-liquid flows have not yet reached the degree of sophistication required to compute phase distributions in complex geometries either in terrestrial or variable gravity conditions. The question is if there will ever be such a general two-phase CFD code that would account for all aspects of flow dynamics and energy transfer. Despite all the objective difficulties, there is a strong need to utilize two-phase gas-liquid flow systems in microgravity environment due to their superior performance compared to the single-phase systems. The terrestrial two-phase flow systems also need optimization that would be based on better understanding of the two-phase flow phenomena.

Two phases of the two-phase gas-liquid system are liquid and gas or void phase. Void fraction is, by definition, the volume of void (gas) phase in a total volume occupied by both gas and liquid. Phase distribution is the instantaneous spatially-resolved distribution of phases (gas or liquid) in a certain geometry. There is a need to measure void fraction on different scales for the whole volume domain accurately, non-invasively, and non-intrusively.

Current measuring techniques are usually intrusive and/or invasive, bulky, tedious, complex, or simply inadequate to capture the dynamics of the flow. Some of the common non-invasive methods use a Photon-Attenuation technique (includes γ-Ray and X-Ray radiation) that rely on the absorption law, $I = I_0 \exp(-\mu_a L)$, for the monochromatic collimated photon beam being attenuated over distance L. Obviously, such techniques can provide only line-averaged void fraction and in some instances area-averaged void-fraction by using multiple photon beams and detectors. The high-energy electron (β-Ray) absorption, neutron scattering, and other particle radiation techniques are based on similar principles ([2, 13]). A large class of experimental techniques are placed in the category of optical methods. Optical techniques require transparency and are plagued with multiple-scattering problems. Then there are probes based on the electrical properties of the multi-phase and/or multi-component mixtures, such as: conductivity, capacitance, impedance, etc. Local probes such as micro-thermocouples, isokinetic probes, hot-wire and hot-film probes, etc. ([2, 13]), are also widely used but are obviously, both, intrusive and invasive, thereby affecting the measured flow. A major perturbation in the flow is caused by holdup technique (which rapidly seals off a section of a channel) which cannot be used for monitoring purposes

but only for gross calibration of other techniques. The discussion of shortcomings and advantages of each technique is beyond the scope of the present work. More information about particular techniques can be found in many references, such as [2, 13].

Magnetic Resonance Imaging (MRI) is a technique based on Nuclear Magnetic Resonance (NMR) and was introduced in the early 70's. While the NMR is mostly used for spectroscopy and relaxometry, the MRI provides additional dimensions and that is imaging or spatially-resolved signals to which many different imaging contrasts can be added. The inherent capabilities of an MRI are to measure the spatial distribution of the nuclear spins and as such needs a set of gradient coils that would, usually linearly, modulate the strong polarizing uniform field. The spatial resolution of the MRI can go down to 1-10 μm while the temporal resolution can be typically on the order of 1-10 milliseconds. Trade off between temporal and spatial resolution is required. The NMR is very insensitive technique with respect to SNR (Signal-to-Noise Ratio), but has a great advantage over all other tomographic techniques (X-Ray CT, etc.) because it provides unsurpassed level of contrasts.

A review of MR imaging techniques as a tool to characterize various single- and two-phase flows is given in a number of excellent papers, such as, *Majors, et al.* (1989) [16], *Caprihan and Fukushima* (1990) [4], *Pope and Yao* (1993) [17], *Gladden* (1994) [11], and *Fukushima* (1999) [10]. Most of the MRI investigations of two-phase flows is based on imaging of particulate flows and concentration measurements. None of the review papers reports any gas-liquid MRI measurements and/or research in the period from 1980 to 1999. The only two reported investigations using NMR (and not MRI) in gas-liquid flows will be discussed now.

The first paper known to us dealing with the use of NMR technique in gas-liquid void fraction measurements was done by *Lynch and Segel* [15] in 1977. The authors have used spectroscopic signal from the CW (Continuous Wave) NMR. Signal obtained is the *Fourier Transform* (FT) of the Free Induction Decay (FID), from the total volume that resulted in the volume-averaged integral-scale (sample-size) void fraction in the similar setup as ours. Air was introduced in a stagnant column of liquid. No spatial information on phase distributions or void fraction was provided as authors have used NMR instead of MRI. Nevertheless, it was an important contribution that proved feasibility in using NMR in characterization of gas-liquid flows. The experimental data show linear relationship for NMR signal intensity and void fraction versus air flow rate. The effect of the spin-lattice relaxation T_1 on the signal decay was investigated as well. The authors have compared their integral void fraction measurements versus air flow rate with the *homogeneous* and *Lockhart-Martinelli* correlations. Authors did not discuss the problem of magnetic susceptibility.

In historically the second paper on NMR use in gas-liquid flows, *Abouelwafa and Kendall* (1979) [1] have used CW (Continuous Wave) NMR spectroscopy to measure the signal intensity from the precessing spins (^{1}H) (protons). In this way they measured in situ the volume fractions and individual flow rates of two-component (water-oil or water-air) mixtures. The main goal of their research was to develop the flowmeter for the multi-phase and/or multi-component mixtures. At the time of our MRI experiments we were unaware of the papers by *Lynch and Segel* or *Abouelwafa and Kendall.*

MRI has been successfully used in many investigations of single- and two-phase fluid flow through porous media. We were motivated to extend the MRI technique to gas-liquid flows in channels. In many ways the void fraction estimation is the inverse problem from the porosity/saturation measurements in porous media flows [5, 7, 8].

THEORETICAL CONSIDERATIONS

Two-Phase flow

Two-Phase gas-liquid flow consists of liquid (holdup) and gaseous/vapor (void) phase. Local or spatially-resolved phase distribution or fraction is designated as α_l for liquid and α_v for gas phase [13]. Since we are interested primarily in the spatially-resolved or integral volume fraction of gas phase, we will use designation $\alpha = \alpha_v$. In general, $\alpha = \alpha(x_i, t)$, i.e., local void fraction is a function of spatial and temporal coordinates. For the void phase, the smallest scale at which one can still assume continuum is on the order of 10 μm. The liquid phase and the phase interface have smallest continuum length scales on the order of 10 nm, i.e., a factor of 1000 smaller than gaseous.

We can now define a local instantaneous void fraction (or phase distribution function):

$$\alpha = \alpha(x_i, t) = \begin{cases} 1 & x_i \in \text{void domain} \\ 0 & x_i \ni \text{void domain} \end{cases} \tag{1}$$

If one could freeze the entire gas-liquid flow for an instant, we could perform volume-averaging or volume-smoothing process by increasing the size of the control volume. That would result in a meso-scale volume δV and the *meso-scale* void-fraction in a finite but small volume δV as a centroid around the point x_i:

$$\epsilon(x_i, t) = \frac{1}{\delta V} \int_0^{\delta V} \alpha(x_i, t)\, dx_i^3 \tag{2}$$

and is a function of time and spatial coordinates. For example, in the next instant different phase component can enter the *Eulerian* volume under consideration and/or phases are spatially distributed at each instant of time. The volume smoothing can go up to the integral scale or sample size resulting in an integral void-fraction:

$$< \epsilon(t) > = \frac{1}{V} \int_0^{V} \epsilon(x_i, t)\, \delta x_i^3 \tag{3}$$

which is the function of time only. This kind of information is accessible to NMR spectroscopy ([9, 10, 11, 15]). On the other hand, MRI can give additional information about the spatially-resolved void fraction, i.e., $\epsilon(x_i, t)$. In Fig. 1, we show schematically the thin cross-section slice

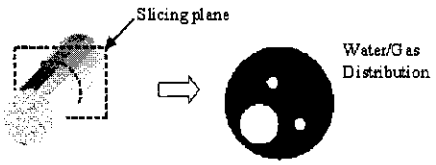

Figure 1: The thin cross-section slice through the test tube with bubbly gas-liquid flow.

through the tube with gas-liquid flow. Area-averaged void fraction can be easily estimated from such images. We can also define a *meso-scale* time τ for the time-averaged void-fraction which will be the function of the spatial coordinate for the fixed *Eulerian* control volume:

$$\overline{\epsilon(x_i,\tau)} = \lim_{\delta t\to\tau}\frac{1}{\delta t}\int_0^{\delta t}\alpha(x_i,t)\,dt \qquad (4)$$

In the case of a quasi-steady gas-liquid flow:

$$\overline{\epsilon(x_i)} = \lim_{\delta t\to\infty}\frac{1}{\delta t}\int_0^{\delta t}\alpha(x_i,t)\,dt \qquad (5)$$

which is the function of spatial coordinates only. Volume-averaging of this time-averaged void fraction results in both time and volume-averaged void fraction:

$$<\bar{\epsilon}>=\frac{1}{V}\int_0^V\overline{\epsilon(x_i)}\,\delta x_i^3 \qquad (6)$$

which one obtains in a steady gas-liquid flow by for example using holdup technique [13, 15]. All the smoothing (integration) techniques could be performed in terms of *Lebesgue* integral which exists even for the domains where the *Riemann* integral is not defined. In the case of steady gas-liquid flow $<\bar{\epsilon}>=\overline{<\epsilon>}$.

While the NMR can only detect volume-averaged (integral) time-resolved void fraction $<\epsilon(t)>$, the MRI can measure both, time- and spatially-resolved void fraction on the meso-scales for time and volume (also area- and line-averages). This inherent ability makes MRI more powerful than any other diagnostic's technique. However, due to the *Fourier imaging* we can not achieve high temporal and high spatial resolution in the same time. Trade off is necessary for the particular case. However, fast imaging techniques such as EPI, FAST, snapshot-FLASH, DANTE, etc., [3] exist and will be explored.

Additional advantage of the MRI is to measure the phase velocities u_i's using the phase-contrast techniques [4, 10, 11, 12, 16, 17]. The volumetric flow rate of each phase is:

$$Q_i = \int_A u_i\,\alpha_i\,dA \qquad i=l,\,v$$

Work is in progress to incorporate phase velocities and phase flowrates measurements with the spatially-resolved void fraction estimations which will be addressed in our subsequent publications.

NMR basics

The Nuclear Magnetic Resonance (NMR) phenomena is based on the non-vanishing quantum magnetic dipole moment of certain nuclei [3, 9, 12, 14]. Proton or ^{1}H which is the member of the *Baryon* family of elementary particles with the mass of 939 MeV is also the most abundant nuclei in nature). It also posses the strongest magnetic dipole moment which is fortunate since water is the most important technical and biological liquid fluid. The magnetic dipole moment $\mu_i = \gamma\,J_i$, where J_i is the nuclear angular momentum or spin and according to the rules of quantum mechanics can only have discrete values. Nuclear magnetic spins are polarized longitudinally in an uniform magnetic field due to the dominant *Zeeman* energy-splitting interaction [3, 9, 12, 14]. For protons, which are also *fermions*, spin quantum number is $\pm 1/2$ and the orientation in a longitudinally polarizing uniform magnetic field B_0 can be spin-up $\uparrow$ (parallel) or spin-down $\downarrow$ (anti-parallel). The parallel orientation is the preferred lower energy level while the anti-parallel configuration represents higher energy level, with energy difference, $\Delta E = -hf_0 = -\hbar\gamma B_0 = -\hbar\omega_0$. NMR and MRI experiments are notoriously insensitive at normal room temperatures because the thermal motion of the lattice will excite roughly half of the spins to "jump" to the higher energy level (anti-parallel $\downarrow$). The *Maxwell-Boltzmann* (MB) classical statistics can be used as a high-temperature asymptotic behavior of the quantum *Fermi-Dirac* (FD) or *Bose-Einstein* (BE) statistical distributions. The FD quantum distribution is correct distribution for *fermions* while the BE distribution is the correct quantum distribution for *bosons*. *Fermions*, such as proton, are elementary particles with half-integer quantum spin number for which *Pauli's exclusion principle* applies and which have anti-symmetric wave function. *Bosons* are elementary particles with integer spin number (or zero) for which *Pauli's exclusion principle* does not apply and which have symmetric wave function. Photon, the carrier of the electromagnetic interactions, is a typical *boson* which populates the same quantum state with other photons, has zero rest mass, and zero quantum spin number.

According to the MB classical distribution the population of parallel spins N_α is related to the number of anti-parallel spins N_β as:

$$\frac{N_\alpha}{N_\beta} = \exp\left(\frac{\hbar\omega_0}{kT}\right) \qquad N_\alpha + N_\beta = N \qquad (7)$$

Since $kT \gg \hbar\omega_0$ at room temperatures (T=300 K), the *Taylor* expansion of the exponential function leads to:

$$\frac{N_\alpha}{N_\beta} = 1 + \frac{\hbar\gamma B_0}{kT} + \mathcal{O}\left[\left(\frac{\hbar\gamma B_0}{kT}\right)^2\right] \approx 1 + 0.679\cdot 10^{-5} B_0$$

where B_0 is the uniform polarizing field in Tesla. Here, $\hbar = h/2\pi$ is the angular *Planck's* constant, $\omega_0 = \gamma B_0$ is the angular nuclear (*Larmor*) resonance frequency, γ is the *gyromagnetic* ratio which is constant $42.58\cdot 2\pi$ rad MHz Tesla^{-1} for ^{1}H, and k is the *Boltzmann's* constant. At room temperature, the MB distribution show that approximately only one in 100 001 spins will actually result in net equilibrium magnetization, all other 10^5 canceling each other. Accordingly, in a population of 10^{20} spins

only about 10^{15} spins will result in a measurable equilibrium magnetization which is why NMR/MRI is greatly insensitive. The relative population difference in high-temperature approximation results in:

$$\frac{\Delta N}{N} = \frac{N_\alpha - N_\beta}{N} \approx \frac{\hbar\gamma B_0}{2\,k\,T} \qquad hf = \hbar\omega_0 \qquad (8)$$

and is a very small number at room temperatures in thermal equilibrium. This is because the lattice is much larger energy reservoir than quantum interactions at room temperatures. The NMR photons are in the radio-range, typically $f = 1 \rightarrow 300$ MHz, and thus of very low ionization energy. The 10 MHz radio-wave has wavelength of approximately 30 meters and its single photon energy is on the order of 10^{-26} J or 10^{-7} eV. That explains why the MRI is so widespread in medical imaging.

The quantum net magnetization in thermal equilibrium for ^{1}H is equivalent to the experimental *Currie's* law:

$$M_0 = \rho_0 \frac{\gamma^2\hbar^2}{4\,k\,T} B_0 \propto \frac{\rho_0\, B_0}{T} \qquad \hbar\omega_0 \ll kT \qquad (9)$$

where $\rho_0 = N/\delta V$ is the spin density. Polarization in uniform magnetic field will, however, take finite amount of time - called T_1 or *spin-lattice* (or longitudinal) relaxation time.

MRI basics

The MRI was "born" in 1973 in seminal and independent papers by *Mansfield* and *Lauterbur* (recipients of the Nobel price in Medicine for 2003). MRI is based on NMR [3, 14] by adding "gradient coils" that can locally modulate the magnetic field and accordingly the local nuclear *Larmor* frequency $\omega(x_i) = \gamma B(x_i)$. This procedure is called frequency (or space) encoding [3, 9, 12]

$$\omega(x_i) = \omega_0 + \gamma \frac{\partial B_0}{\partial x_i} x_i = \omega_0 + \gamma\, G_{x_i} \cdot x_i \qquad (10)$$

where $\mathbf{B_0}$ is a *solenoidal* field $\nabla \cdot \mathbf{B_0} = 0$, and is also irrotational in the case there are no conductors inside the sample, i.e., $\nabla \times \mathbf{B_0} = 0$. The difference of volume magnetic susceptibility between two adjacent media (air/water interface) gives rise to distortions in the local magnetic field and thus to image artifacts. These distortions may be detrimental in imaging but can provide useful information about material inhomogeneity. The susceptibility χ is a dimensionless tensor, which relates the contribution of the magnetic polarization $\mathbf{M}_p$ of matter to the magnetic field $\mathbf{H}$ applied in vacuum, so that magnetic induction $\mathbf{B}$ in matter can be written as:

$$\mathbf{B} = \mu_0(1+\chi)\cdot\mathbf{H} = \mu_0(\mathbf{H}+\mathbf{M}_p) \qquad \mathbf{M}_p = \chi\,\mathbf{H}$$

We used Spin-Echo (SE) imaging [3, 12, 14] for the void fraction measurements. SE imaging in a gradient field results in a spatially-resolved MRI intensity, i.e., the signal intensity from each voxel, which size can be changed, is distributed throughout the sample. The MRI spin-echo measurement yield the intensity of the NMR signal that is proportional to the spin density of the precessing protons in each voxel. The amount of water in each voxel is directly proportional to the NMR signal intensity coming from that voxel.

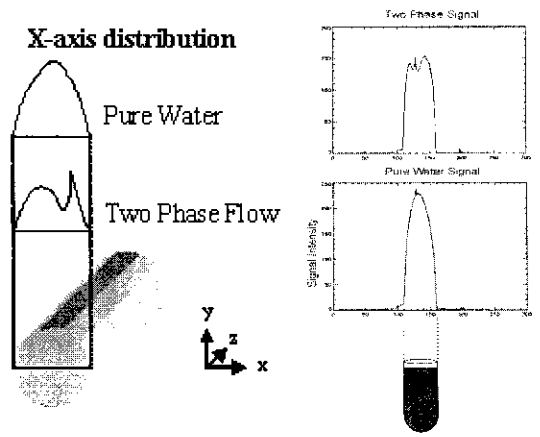

Figure 2: 1D x-axis cross-sectional spin-density distribution in a cylindrical tube. Void fraction was averaged in a longitudinal z and y direction. Void fraction distributions were obtained by subtracting two-phase flow signal from the single-phase water signal (left). Difference in NMR/MRI signals for the single-phase and two-phase flow averaged void fraction distribution in a vertical tube with stagnant liquid at 30 ml/min air flow rate (right).

The spatial resolution of MRI, $1/\Delta x_i$, is related to NMR absorption line width or spread in *Larmor* frequencies and is reasonably high in liquids:

$$\left|\frac{1}{\Delta x_i}\right| = \left|\frac{\gamma\, G_{x_i}}{2\pi\Delta f}\right|$$

The NMR signal intensity coming from the voxel filled only with water has maximum intensity, I_{ref}. The NMR signal coming from the voxel on the meso-scale is $I_0(x_i,t) < I_{ref}$. The local quasi-instantaneous void fraction is then:

$$\epsilon(x_i,t) = \frac{I_{ref} - I_0(x_i,t)}{I_{ref}} = 1 - \frac{I_0(x_i,t)}{I_{ref}} \leq 1 \qquad (11)$$

where the ratio $I_0(x_i)/I_{ref}$ represents the liquid hold-up. In Fig. 2, the cross-sectional longitudinally-averaged void fraction distribution is shown schematically. The estimation of the local void fraction in this way is straightforward. However, there are a few problems. One is the inevitable attenuation of the signal and the inability to measure the spin-density at the time zero or at the moment immediately following the tipping of the longitudinal magnetization. The first SE will yield smaller amplitude than the signal that would be coming from all in-phase precessing nuclei at the time equal zero. The reason for this signal attenuation is in the irreversible, energy-conserving, *spin-spin* or T_2 (transverse) relaxation. The single SE intensity is therefore only a fraction of the original signal at time equal zero. Therefore, one has to repeat the SE experiment for different echo times and then fit and extrapolate the signal to time zero. This technique is called Multiple Spin-Echo imaging (MSE) [7, 8] It should not be confused with the classical CPMG (*Carr-Purcell-Meiboom-Gill*) or *echo-train* method [3, 9, 12] used to estimate T_2 relaxation.

Sample was positioned in the *rf* (radio-frequency) coil inside the MRI and spins were polarized in a uniform B_0 field after approximately $5\,T_1$'s. Then the equilibrium lon-

gitudinal magnetization is tipped by a weak B_1, *rf* $\pi/2$-pulse, at exactly the nuclear (*Larmor*) frequency, hence Magnetic Resonance. Precessing nuclei are inducing FID (Free-Induction-Decay) signal on the receiving coil. After time $t_E/2$ the π-pulse in the transverse plane is applied to rephase the spins. The flip angle θ can be estimated from the tipping *rf* pulse B_1 of duration τ as: $\theta = \gamma B_1 \tau$.

Right after the $\pi/2$-pulse all components of the transverse magnetization are precessing with approximately the same phase. The net magnetization undergoes a coherent rotation. As a result of inevitable inhomogeneities in the local magnetic fields (T_2^* relaxation), the coherence of rotation is lost due to the appearance of the different precession phases. Thus, the vector sum of all transverse magnetization components eventually vanishes. But as long as the precession frequency of each magnetization frequency remains unchanged, a simple permutation (time reversal) of the fast versus slow components will generate the reoccurrence of the signal after another time $t_E/2$. That permutation is achieved by the π-pulse. Accordingly, an echo of the FID signal will appear after the time corresponding to twice the pulse separation time [3]. This time t_E is called *Echo time* in imaging.

In the center of the Spin or *Hahn* echo, all magnetization components are refocused. Since the echo amplitude is smaller than the original amplitude at time equal zero it will look as if there are less ^{1}H nuclei in the voxel leading to void fraction overestimation. We are therefore using MSE [7, 8] to reconstruct the voxel's proton density.

The NMR SE intensity is proportional to the echo-time t_E,

$$I_{SE} = I_0 \exp(-t_E/T_2) \tag{12}$$

where, I_0 is the unknown initial equilibrium magnetization (to be extrapolated) and obtained on the *rf* coil just after the $\pi/2$-pulse. Actually, there is a slight delay of 10-20 μs before the receiving signal is picked up in the *rf* coil due to the transmit-receive switch inertia. If, for example, we conduct two spin-echo experiments with variable echo-times t_{E1} and t_{E2} the corresponding spin-echo intensities will be I_{SE1} and I_{SE2}. Assuming a single-exponential decay, Eq. (12), one can estimate the transverse relaxation time

$$T_2 = (t_{E2} - t_{E1}) \,/\, \ln \frac{I_{SE1}}{I_{SE2}} \tag{13}$$

and the initial magnetization (spin density) is then simply

$$I_0 = I_{SE1} \exp(t_{E1}/T_2) \qquad I_{SE1} < I_0 \tag{14}$$

For better accuracy and statistical confidence several SE tests with different echo-times were performed and the I_0 was extrapolated by single-exponential fit using the Least-Squares fitting.

The detected MRI signal in the **k**-space is the FT of the spatial spin density $\rho(x_i)$, also known as the 3D-imaging equation [12]:

$$s(k_i) = \iiint d^3x_i \, \rho(x_i) \, e^{-i2\pi k_i \cdot x_i} \tag{15}$$

Reconstructed image is obtained from the *inverse Fourier Transform*:

$$\rho(x_i) = \iiint d^3k_i \, s(k_i) \, e^{+i2\pi k_i \cdot x_i} \tag{16}$$

Time-dependent component of the wave vector k_i, which is also the *Fourier-conjugate* variable to the position vector x_i, is:

$$k_i(t) = \frac{\gamma}{2\pi} \int_0^t G_i(\tau) d\tau \qquad G_i = \frac{\partial B_0}{\partial x_i} \tag{17}$$

In *spin-warp* imaging used here the signal intensity depends on the repetition time t_R and the echo time t_E of successive scans. The initial longitudinal magnetization $M_z(\mathbf{r})$ depends on T_1 relaxation time. Relaxation-time contrast can be applied to signal coming from each voxel location $\mathbf{r}$, resulting in weighted signal:

$$M(\mathbf{r}, t_R, t_E) = M_0(\mathbf{r}) \left\{ 1 - \exp\left[-\frac{t_R}{T_1(\mathbf{r})} \right] \right\} \exp\left[-\frac{t_E}{T_2(\mathbf{r})} \right]$$

where $M_0(\mathbf{r})$ is the thermodynamic equilibrium magnetization according to *Currie* law, Eq. (9).

Three gradients are applied in the 2D FT *spin-warp* imaging [3, 4]. One is the *slice-selection* gradient G_z, then *phase-encoding* gradient G_y for a fixed time interval, and finally *read-out* gradient G_x and acquisition of n data points. *Phase-encoding* gradient is then incremented and the whole procedure repeated $m-1$ times after which a 2D FT of the $n \times m$ data matrix is performed for image computation. To prevent signal aliasing by frequency folding during detection *Nyquist* sampling frequency must be used.

EXPERIMENTAL SETUP

Our MRI system, shown in Fig. 3, is based on a 1900 lbs (865 kg) NdFeB low-field 0.267 Tesla (2670 Gauss) permanent-magnet protected by the *Faraday* cage. Very low fringe (stray) magnetic field exists which minimizes the *rf* disturbances and relaxes the safety considerations. The static magnetic field is very homogeneous due to the four large (110 cm) return pole pieces that also minimize stray field. The health hazard limit of 5 Gauss is almost contained within the main body. The operating proton frequency is about 11.3 MHz, which is outside the public FM range (it is in the HF range). Homogeneous region of 8 cm DSV exists with the homogeneity of 25 ppm p-p. Clear access of 13.6 cm exists in which the measuring sample, gradient coils and the *rf* probe-transmitter is placed. The resistivity of the pole pieces is larger than 1.2 μOhm meter. The large magnet mass has a long temperature stabilization time and requires conditioned air with temperature control within $2-3$ K for the stability of the static field. Intel Pentium PC computer with the I/O Texas Instrument TMS 320 C044 60 MHz DSP is used. Full functioning and flow imaging optimized Image-processing and spectroscopic analysis software is installed. Image processing software is IDL 5.6. Details about the NASA's MRI test rig can be found in *Daidžić et al.* [7, 8]. Detailed information on the NMR/MRI hardware can be found in [3, 9, 12].

All of the experiments employed SE's. The shortest echo time was 6 ms. For projection imaging, broadband (or

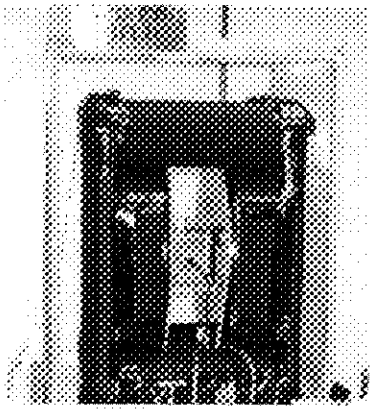

Figure 3: NASA GRC's 0.267 Tesla MRI facility.

hard) *rf* pulses of duration 120 μs were used. For slice selection, 5-lobe *sinc* amplitude modulated pulses of duration 1 ms were used. Two dimensional FT imaging was done with standard *spin-warp* sequences with imaging gradients of up to 1.9 G/cm. For quasi-steady flows we repeated the measurements $n = 2 \rightarrow 4$ times as the SNR$\propto \sqrt{n}$. The NMR signal intensity is $\propto \gamma^3 B_0^2 \rho_0 / T$ [12]. In our MSE experiments, echo-time was changed from 6 ms up to several tens of milliseconds. Criterion for acceptable extrapolation was that I_{SE1} had to be at least 80% of extrapolated I_0, and more than 6 different SE amplitudes must have been obtained. Minimum echo amplitudes used in fitting were larger than 20% of I_0. Water was doped with small concentration of $CuSO_4$ para-magnetic salt to reduce longitudinal relaxation.

Susceptibility mismatch across the air-water interface induces frequency shift. The image distortions around the interface will depend on the tensorial properties of the susceptibility difference. For imaging with *spin-warp* a definite distortion of the image around the interface will occur. The frequency shifts caused by susceptibility mismatch can be resolved with spectroscopic imaging [3]. Air largely consisting of nuclei with zero magnetic dipole moments is transparent to NMR signal and only precessing ^{1}H induce *emf* in the receiving coil by the law of *Faraday*:

$$\text{emf} = -\frac{d}{dt} \int_{\text{Coil Area}} \mathbf{B} \cdot \mathbf{ds}$$

Accordingly, we measure gas phase (void) distribution indirectly through the measurement of liquid holdup, Eq. (11). The spatial signal is compared to a test tube filled with water to extract the gas-phase distribution. Fast temporal measurements of phase distributions in cross-section of the tube and time-averaged void fraction for the 2D and 3D domains in case of a steady flow have been obtained. Due to the relatively fast echo sequencing and low bubble velocities good spatial and temporal resolution was achieved at lower flow rates. The characteristic voxel size was on the order of 500 μm (0.5 mm). The spatial resolution can be improved down to 250 μm, in which case the temporal resolution would suffer.

RESULTS AND DISCUSSION

Nonconducting tube 20 cm long and 2.5 cm in diameter, shown in Fig. 5 (right), was placed in a 10 cm ID solenoidal *rf* coil of the MRI and an accurate syringe pump was delivering air flow in upward direction at the rate varying from 1 to 200 ml/min. In figure 4, the procedure for void fraction calculation from the spatial MRI signal is shown (see also Fig. 2). The two-phase flow signal is subtracted from water signal, voxel by voxel, resulting in void fraction for each *meso-scale* voxel, Eq. (refeg:mesoscale).

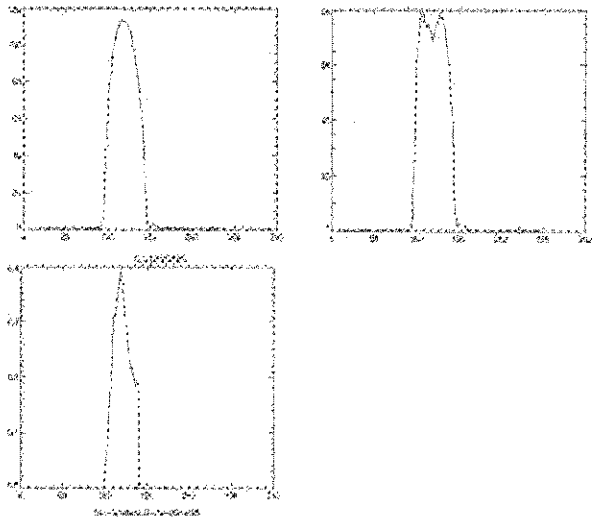

Figure 4: Difference in NMR/MRI signals for the single-phase and two-phase flow averaged void fraction distribution in a vertical tube with stagnant liquid at 30 ml/min air flow rate.

The volume- and time-averaged void-fraction $< \bar{\epsilon} >$ can be estimated for not too large air flow rates by measuring the height of the stagnant liquid column l_0 and height of the column when two-phase flow exists $l_1 > l_0$, as shown in Fig. 5, resulting in:

$$< \bar{\epsilon} > = 1 - \frac{l_0}{l_1} \qquad \Delta V = (l_1 - l_0)\frac{D^2 \pi}{4} \qquad (18)$$

Integral void fraction calculated from the ratio of column heights from Fig. 5, for air flow rate of 30 ml/min is 0.11 ± 0.01 by using Eq. (18). The void fraction obtained by averaging in two-different dimensions, Figs. 8 and 9, show from the linear approximation at 30 ml/min air flow rates void fractions very close to 0.11 which confirms the visualization result. Unlike in [15], we do not need a (CCD) camera nor any optical access as the MR imaging capabilities are used for that purpose, although camera can be used for independent verification.

Using the thin cylindrical slice perpendicular to tube's longitudinal axis the cross-sectional holdup distribution is shown in Fig. 6 (left) for 30 ml/min air flow rate. Cross-sectional void fraction can be easily extracted from here.

In Fig. 6 (right), a 3D image of gas-liquid flow is shown. The blue-scale variation represents the void-fraction variation in different cross-sections. Since the creation of such a 3D image with high spatial resolution takes long time (order of minute) it is necessary that the flow is quasi-steady. Each voxel's void fraction is time-averaged according to Eq. (5). In Fig. 7, the projections of the 3D image of two-phase flow void-fraction distributions are

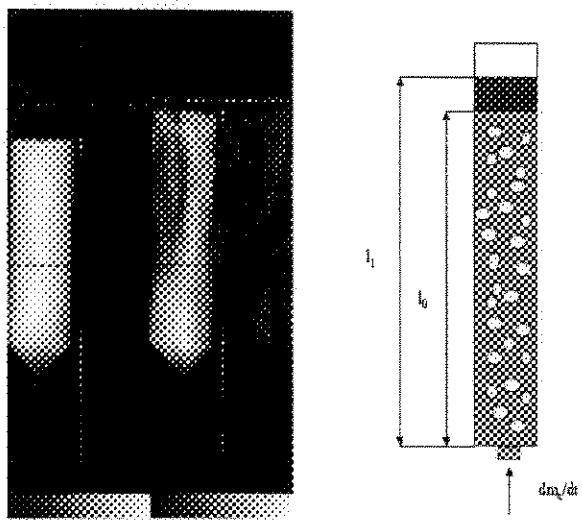

Figure 5: Side by side 2D images of the stagnant single-phase (water only) and the two-phase (water-air) flow at 30 ml/min air flow rate. The gray scales are representative of signal intensity (left). The schematic drawing of the test tube with stagnant liquid through which air was introduced is placed in the *rf* coil of MRI (right).

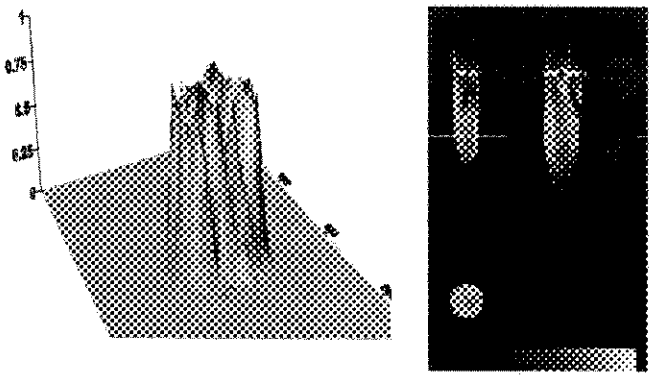

Figure 6: Instantaneous 2D cross-section distribution of thin-slice longitudinally-averaged liquid holdup in a vertical tube with stagnant liquid at 30 ml/min air flow rate (left). 3D image for the particular slice of the spatially-resolved time-averaged void fraction for a vertical tube (right).

shown. The flow occurs at high flow rate > 150 ml/min. It is easy to see how the liquid film is contained at the wall forming annular flow conditions while the core of the cylindrical tube has high, and more or less uniform, void fraction distribution. It is expected that the gas-liquid flow in vertical flows with $\epsilon > 0.20$ will transition to slug and churn flow (bubbly annular transition).

In Fig. 8, the variation of the void fraction with the flow rate ($1 - 140$ ml/min) is shown. The change is nearly linear for lower flow rates but for the higher low rates the MRI signal changes non-linearly and starts even decreasing for (> 180 ml/min). The reason for such behavior at high flow rates is the T_1 relaxation effects and the short resident time of spins in voxels. The way to deal with this problem is to differentiate between stationary and moving spins. The integral void fraction was obtained by averaging void fraction along the tube's length and then averaging along the y-axis resulting in the x-axis distribution. In the next

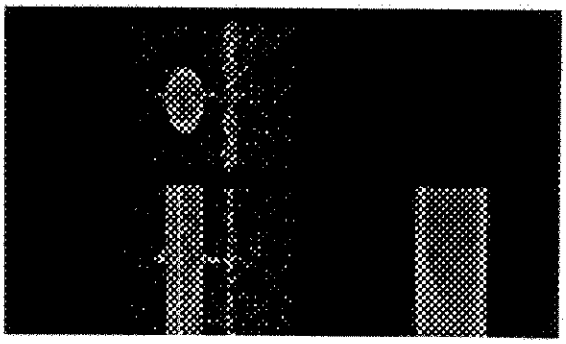

Figure 7: 3D image for high air flow rate.

figure, the distribution will be along y-axis, meaning that the results should be equivalent. However, discrepancies are possible due to misalignment, imaging sequence, gradient strength's, and especially different concentrations of $CuSO_4$ para-magnetic salt.

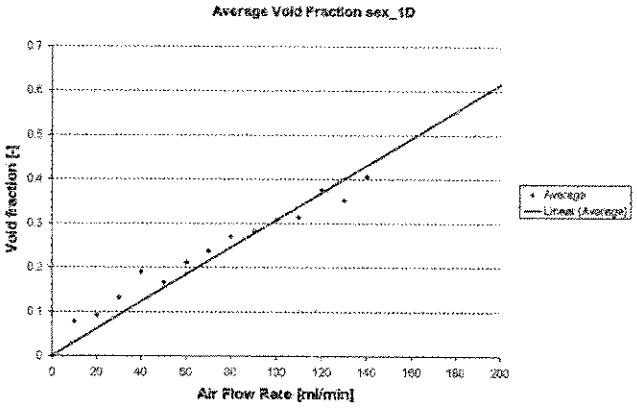

Figure 8: Change of longitudinally (z-axis) and x-axis averaged void fraction as a function of air flow rate. Linear approximation shows reasonable trend. Large deviations appeared for higher flow rates. Errors estimated to ±15%.

In Fig. 9, the variation of the void fraction with the air flow rate (1-200 ml/min) is shown. The change is nearly linear for lower flow rates but for the higher flow rates (> 140 ml/min) the MRI signal changes non-linearly. We already explained some of the reasons. Without the velocity information it is impossible to say just what should be the slope of the $d\epsilon/dm_a$ gradient. The mass balance can not be closed by void fraction measurements alone. For very high flow rates the magnetic susceptibility effects, aperture error, and T_1 relaxation become significant. Better and faster imaging sequences will be used in the future to deal with such difficulties. Another problem in our imaging efforts is that the bubble formation was not steady but random. MRI was set to perform scanning in fixed intervals so that spatial aliasing could have occured. The bubble's initial velocity and size were also variable and changing in upward direction. Bubbles experienced highest acceleration at the formation site. This is also visible from Fig. 5 as the used MR imaging sequence did not characterize this region well.

CONCLUSIONS

We demonstrated that MRI is a promising non-invasive and non-intrusive technique for experimental estimation

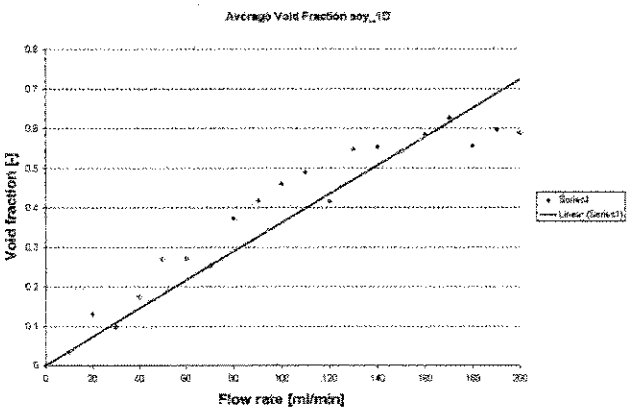

Figure 9: Change of longitudinally (z-axis) and y-axis averaged void fraction as a function of air flow rate. Linear approximation shows reasonable trend up to maximum air flow rates of 200 ml/min. Errors estimated to ±15%.

of the spatially-resolved void-fraction. Also instantaneous or time-averaged void-fraction distributions in cross sections and flow patterns visualization in single- and multi-dimensional spatial domains is possible. We believe that void fractions up to 0.6 were estimated accurately with present imaging techniques. MR imaging has its inherent limitations in low sensitivity and is restricted to lower phase velocities. It needs non-conducting container walls and the image distortions due the magnetic susceptibility at the gas-liquid interface is present. A compromise can be reached between the spatial and temporal resolution. MRI is especially well suited for 3D/2D time-averaged spatially-resolved void fraction measurements in the case of steady two-phase flows or for the fast time-resolved 1D void fraction distribution measurements. Gas-liquid flows can be imaged in adiabatic as well as in diabatic conditions enabling the visualization of the void fraction change along the channel as the heat flux is applied. Another advantage of the MRI is that phase velocity measurements can be added by which independent closure of the mass and momentum balances can be obtained from the MRI measurements alone. Additional improvements can be obtained by using different MRI contrast capabilities to visualize particular transport phenomenon. The problem of magnetic susceptibility mismatch and image distortions in *spin-warp* imaging will be addressed by using spectroscopic imaging with phase encoding technique. More testing with different configurations, geometries, and flow parameters is required.

References

[1] Abouelwafa M.S.A., Kendall E.J.M. (1979) *Optimization of continuous wave nuclear magnetic resonance to determine in situ volume fractions and individual flow rates in two component mixtures* Rev.Sci.Instrum., Vol. 50, 12, pp. 1545-1549

[2] Bergles A.E., Collier J.G., Delhaye J.M., Hewitt G.F., Mayinger F. *Two-Phase Flow and Heat Transfer in the Power and Process Industries* Hemisphere Publishing Corporation, Washington, 1981

[3] Blümich B. *NMR Imaging of Materials* Oxford Science Publications, Clarendon Press, Oxford, 2000.

[4] Caprihan A., Fukushima E. (1990) *Flow Measurements by NMR* Physics Reports (Review Section of Physics Letters), Vol. 4, pp. 195-235

[5] Caprihan A., Daidžić N.E., Fukushima E., Codd S., Alexander J.I.D. (2001) *MR imaging of wetting front dynamics: The effect of gravity* In Proc: 6^{th} International Conference on Magnetic Resonance Microscopy, Jubilee Campus, University of Nottingham, Nottingham, UK, September 2001

[6] Daidžić N.E. (1990) *Basic Equations of Two-Phase (Gas-Liquid) Flow and Interfacial Transfer Terms Modeling* Lehrstuhl für Strömungsmechanik, Universität Erlangen-Nürnberg, Erlangen, 1990

[7] Daidžić N.E. , S. Altobelli, A. Caprihan, E. Schmidt, J.I.D. Alexander (2002) *Estimate of Porosity length-scales in soils by MRI for microgravity plant growth experiments*, in: Proc. 6^{th} International Conference on Magnetic Resonance in Porous Media, September 8-12, 2002, Ulm, Germany

[8] Daidžić N.E., Schmidt E., Altobelli S., Alexander J.I.D. (2003) *Estimate of Porosity Length-Scales in Soil Porous Media by MRI* In Proc: ISSM-IV (Fourth International Symposium on Scale Modeling), September 17-19, 2003, Cleveland, OH, USA

[9] Fukushima E., Roeder S.B.W. *Experimental Pulse NMR: A Nuts and Bolts Approach* Perseus Books Publishing, L.L.C., Cambridge, 1981.

[10] Fukushima E. (1999) *Nuclear Magnetic Resonance as a Tool to Study Flow* Annu. Rev. Fluid Mech., Vol. 31, pp. 95-123

[11] Gladden L.F. (1994) *Nuclear Magnetic Resonance in Chemical Engineering: Principles and Applications* Chem. Eng. Sci., Vol. 49, No. 20, pp. 3339-3408

[12] Haacke E.M., Brown R.W., Thompson M.R., Venkatesan R. *Magnetic Resonance Imaging: Physical Principles and Sequence Design* John Wiley & Sons, Inc., New York, 1999

[13] Hsu Yih-Yun, Graham R.W. *Transport Processes in Boiling and Two-Phase Systems* Hemisphere Publishing Corporation, Washington, 1976

[14] Kimmich R. *NMR - Tomography, Diffusometry, Relaxometry* Springer-Verlag, Berlin, 1997

[15] Lynch G.F., Segel S.L. (1977) *Direct Measurement of the Void Fraction of a Two-Phase Fluid by Nuclear Magnetic Resonance* Int.J.Heat Mass Transfer, Vol. 20, pp. 7-14

[16] Majors P.D., Givler R.C., Fukushima E. (1989) *Velocity and Concentration Measurements in Multiphase Flows by NMR* Journal of magnetic Resonance, Vol. 85, pp. 235-243

[17] Pope J.M., Yao S. (1993) *Quantitative NMR Imaging of Flow* Concepts in Magnetic Resonance, Vol. 5, pp. 281-302